

Optics Letters

1.55 μm band low-threshold, continuous-wave lasing from InAs/InAlGaAs quantum dot microdisks

SI ZHU,^{1,†} BEI SHI,^{1,†} YATING WAN,¹ EVELYN L. HU,² AND KEI MAY LAU^{1,*}

¹Department of Electronic and Computer Engineering, Hong Kong University of Science and Technology, Clear Water Bay, Kowloon, Hong Kong, China

²School of Engineering and Applied Science, Harvard University, Cambridge, Massachusetts 02138, USA

*Corresponding author: eekmlau@ust.hk

Received 17 October 2016; revised 12 January 2017; accepted 13 January 2017; posted 17 January 2017 (Doc. ID 278755); published 6 February 2017

InAs/InAlGaAs quantum dot active layers within microcavity resonators offer the potential of ultra-low-threshold lasing in the 1.55 μm telecom window. Here, we demonstrate the first quantum dot microdisk laser with single-mode emission around 1.55 μm under continuous-wave optical pumping up to 170 K. The extracted threshold is as low as 32 μW at 77 K. This result lays the foundation of an alternative to quantum-well microlasers for low-threshold and highly compact monolithically integratable light emitting sources in fiber communication. © 2017 Optical Society of America

OCIS codes: (140.5960) Semiconductor lasers; (140.3948) Microcavity devices; (230.5590) Quantum-well, -wire and -dot devices.

<https://doi.org/10.1364/OL.42.000679>

Featured with high quality factor (Q), small mode volume, and strong optical confinement, whispering-gallery mode (WGM) semiconductor microdisk (MD) cavities offer the prospect of realizing low-threshold lasers [1], with great potential for integration and low-power operation required for large-scale photonic integrated circuits (PICs) [2,3]. So far, microdisk lasers incorporating quantum-well and -wire active materials have demonstrated excellent device performances [4–13]. The combination of MD with self-assembled III–V quantum dots (QDs) benefits from the carrier localization/confinement in QDs while minimizing carrier diffusion and surface recombination at the disk sidewall. In the perspective of miniaturized ultra-low-threshold and temperature-insensitive lasing devices [14], QD lasing from microdisk structures has been reported for various material systems [15–18]. To date, the emission wavelength of QD microdisk lasers (MDLs) ranges from 1300 nm by In(Ga)As/(Al)GaAs [15,16] to 430 nm by InGaN/GaN [17]. However, few investigations on QD microdisk lasing in the C-band range (1530–1565 nm) have been reported, which is crucial to fiber-optic communications [18].

In this work, we incorporate seven-stack InAs/InAlGaAs quantum dots as the active region in high Q (~ 3835) microdisk cavities with a diameter of 4 μm . Continuous-wave (CW), single-mode lasing at 1.54 μm was observed at 77 K with a threshold as low as 32 μW ($\sim 250 \text{ W}/\text{cm}^2$). To the best of our knowledge, this is the first demonstration of lasing behavior from microdisk cavities incorporating QDs active regions in the conventional C-band window. These results represent a significant progress in realizing low-threshold quantum dot microlasers for transmission in fiber communication and optical interconnects for dense photonic integration.

The epitaxial growth of the microdisk laser was performed in an AIX 200/4 metalorganic chemical vapor deposition (MOCVD) system. Figure 1(a) illustrates the schematic diagram of the fabricated microdisk laser structure. The disk region consists of seven-layer well-layered InAs QDs separated by 50 nm $\text{In}_{0.51}\text{Al}_{0.29}\text{Ga}_{0.2}\text{As}$ spacers, sandwiched by two symmetrical 70 nm thick $\text{In}_{0.51}\text{Al}_{0.49}\text{As}$ cladding layers [19]. A uniform QDs distribution with high QD density is shown in the 1 $\mu\text{m} \times 1 \mu\text{m}$ atomic force microscopy (AFM) scan in Fig. 1(b). The average QD density was counted to be $\sim 5 \times 10^{10} \text{ cm}^{-2}$, without any obvious large coalesced islands, indicating minimal defect formation within the QD layers. To further evaluate the optical potential of these multilayer QDs, power-dependent microphotoluminescence ($\mu\text{-PL}$) at liquid nitrogen temperature (77 K) was conducted, as depicted in Fig. 1(c). In the low excitation power regime (10 μW),

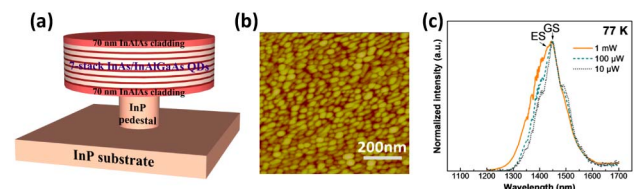


Fig. 1. (a) Schematic illustration of the fabricated microdisk structure showing the epi-layers. (b) AFM image of a single layer QD, with excellent uniformity and high density. (c) Normalized power-dependent photoluminescence of the as-grown sample at 77 K.

ground-state (GS) emission at $\sim 1.45 \mu\text{m}$ was identified. The shoulders appearing at each side of the spectrum suggest some inhomogeneity of the InAs QDs. With excitation power increased to $\sim 1 \text{ mW}$, the first excited state (ES) started to emerge, together with an inhomogeneous broadening.

Colloidal lithography was adopted to ensure perfect circularity of the disks. 200 nm SiO_2 was deposited onto the as-grown sample by Plasma Enhanced Chemical Vapor Deposition (PECVD), serving as hard masks instead of photoresist, for reduced mask erosion during the dry-etch step [20], thus providing a smoother sidewall. $4\text{-}\mu\text{m}$ -diameter silica beads diluted in isopropyl alcohol (IPA) were dispersed onto the sample surface by a micropipette. The sample was then rapidly dried on a 110°C hotplate, leaving isolated beads adhered onto the oxide hard mask. Reactive Ion Etching (RIE) was utilized to transfer the perfectly round pattern to the oxide in an O_2/CHF_3 ambient, followed by silica bead removal with acetone in an ultrasonic bath. An Inductively Coupled Plasma (ICP) etch was performed with an Ar and BCl_3 mixed gas system to reach a depth of $\sim 1 \mu\text{m}$ into the epi-structure, exposing the InP post region. The ICP chamber was maintained at a pressure of 5 mTorr and an elevated substrate temperature of 30°C . An imperfect etched sidewall may result in large scattering loss and nonradiative recombination, hindering the device from lasing. Therefore, optimized dry etching plays a key role in obtaining a smooth disk sidewall with a round shape and a vertical profile. Subsequently, to assure superior mode confinement in the periphery of the active region, as well as to maintain a good thermal conductivity from the disk to the substrate underneath, the InP substrate was laterally etched in part to form a pedestal, supporting the disk membrane. A $\text{HCl}:\text{H}_2\text{O} = 1:1$ solution was used as the highly selective etchant for forming the pedestal. Finally, the SiO_2 hard mask was removed by a buffered oxide etch (BOE). Figures 2(a) and 2(b) present a 70° tilted scanning electron microscope (SEM) image of the whole device topology and a close-up view of the disk sidewall, revealing a steep and smooth sidewall, crucial to the quality of resonant modes. Figure 2(c) exhibits the top-down SEM image of the fabricated MDL, demonstrating its circular geometry. From measurements of the top-down SEM images, we found that the disk diameter varies from $\sim 3.5 \mu\text{m}$ to $\sim 4.2 \mu\text{m}$, because of the size variation of the commercial beads and disk shrinkage introduced by the dry-etch process.

Lasing characteristics of the fabricated devices were measured in a confocal $\mu\text{-PL}$ setup. Samples were mounted in a cryostat with constant nitrogen gas flow. Individual MDL was optically pumped by a CW Ar ion laser operating at 514 nm . The focused spot with a diameter of approximately

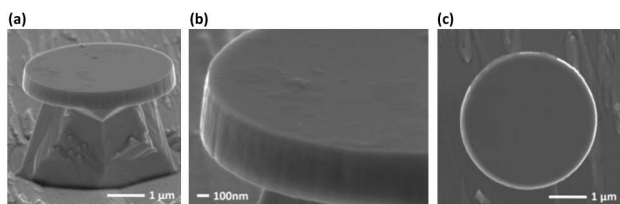


Fig. 2. SEM images of a $4 \mu\text{m}$ microdisk. (a) 70° tilted view of the whole device. (b) Zoom-in image of disk sidewall, showing vertical profile and smoothness. Seven-stack QDs can be recognized faintly by different gray contrast. (c) Top-down view implying good circularity.

$4 \mu\text{m}$ was aimed at the edge of the disk. We assume that $\sim 60\%$ of the power reaching the sample surface was effectively absorbed, considering multiple absorptions/reflections in the disk [21,22]. The output emission was collected from the top surface of a single MDL, dispersed via a monochromator with an 830 l/mm grating (spectral resolution of 0.11 nm), and detected by a thermoelectric-cooled InGaAs detector. To assure the spatial stability of pumping over time, careful alignment was performed to ensure a maximum output with the same input at the beginning of each measurement.

Lasing behavior was first characterized at liquid nitrogen temperature (77 K). Representative single-mode lasing spectra from a $4 \mu\text{m}$ disk are demonstrated in Fig. 3(a). At low pump level, the emission from the InAs QDs in the disk shows a strong transverse electric (TE)-polarized WGM at a wavelength of 1534 nm , accompanied by other weak cavity modes. As pumping power gradually increased, the mode at 1534 nm dominated and eventually lased. Peaks of higher-order modes became conspicuous at higher pump levels. No saturation trend appeared, even for high injection power at three times the threshold. And a high extinction ratio of $\sim 24 \text{ dB}$ was observed when the pumping power tripled the threshold power. Figure 3(b) presents the linear plot of output intensity versus input power (L–L curve) of the lasing mode, where the pronounced kink signified the onset of lasing. The threshold was extrapolated to be around $32 \mu\text{W} \pm 1.3 \mu\text{W}$ by linear fitting of the L–L curve above threshold. A log–log L–L curve is shown in Fig. 3(c), showing the transition from spontaneous emission to stimulated emission until lasing as indicated by the “S-shape” of the curve. By fitting the experiment data with rate equations [22–25], the spontaneous emission coupling factor (β) is extracted to be ~ 0.5 . The high β value suggests that a large fraction of spontaneous emission was coupled into the lasing mode, further favoring the low threshold.

Since the disk was undercut by approximately $1 \mu\text{m}$ from the periphery, higher radial-order WGMs were concentrated spatially closer to disk center and leaked through the InP pedestal. Only the lowest-order WGMs can be sustained and oscillate in the periphery. Carriers generated in the periphery of the microdisk have a much higher chance of radiative recombination and coupling with first-radial-order WGMs, which possess the highest Q -factors and are the most favorable for lasing [26,27]. The free spectral range (FSR) of the first-radial order WGMs can be calculated by $\Delta\lambda = \lambda^2/2\pi r n_{\text{eff}} = \sim 55 \text{ nm}$, where λ is the emission wavelength, r is the disk radius, and n_{eff} is the group effective refractive index. As shown in Fig. 4(a), the mode spacing between the lasing mode and its adjacent higher and lower modes in the same radial order are 55.4 nm and 55.8 nm , respectively. This agrees well with the theoretically predicted result. Meanwhile, the relative intensity of the resonant mode at 1534 nm exhibits a pronounced increase from $0.8 \times P_{\text{th}}$ to $1.3 \times P_{\text{th}}$, illustrating the behavior near the lasing threshold. Figure 4(b) depicts a bi-Lorentzian fit to the sub-threshold emission at $0.8 \times P_{\text{th}}$. The blue line matches the broad InAs QDs background emission and the orange line corresponds to the narrow cavity emission. The inset is an expanded spectrum of the shaded region with a tri-Lorentzian fit, indicating a full width at half-maximum (FWHM) of the 1534 nm mode to be 0.4 nm . Hence, the cold cavity Q -factor of the lasing mode can be extracted to be ~ 3835 at transparency, corresponding to a cavity finesse

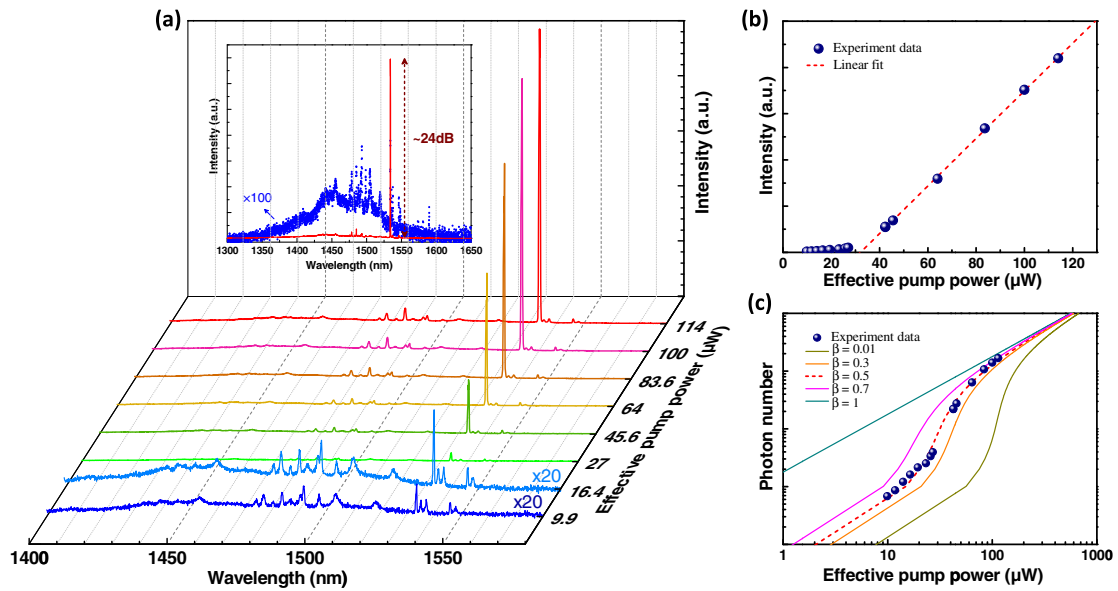


Fig. 3. Lasing operation of a 4 μm diameter microdisk at 77 K. (a) Power-dependent $\mu\text{-PL}$ spectra. Spectra at low pump level (9.9 and 16.4 μW) are magnified 20 times to illustrate the broad spontaneous emission from the QDs. Insert: overlay of spectra measured below (blue dot, 9.9 μW , amplified 100 times) and above (red line, 114 μW) threshold. (b) L-L curve in linear scale. The dashed red line represents a linear fit to the experiment data. The threshold is extrapolated to be 32 μW according to the fit. (c) L-L curve in log-log scale. Rate equation model solutions for various values of β are represented as solid lines. The best fit suggests a high β value of 0.5.

of $F = \text{FSR}/\Delta\lambda = 137.5$, which is 13 times larger than what was reported in Ref. [5]. Furthermore, this cold cavity Q -factor is the highest among other quantum-well microdisk lasers in the same wavelength range [2,7,8,10,12]. The high quality factor can be attributed to the smooth sidewall and perfect circularity of the fabricated disks. Combining the incorporation of QDs as the lasing medium resulted in extremely low threshold of the laser.

Temperature characteristics of the 4 μm diameter MDLs were also studied. Figure 5(a) compares the normalized lasing

spectra above threshold ($\sim 1.3 \times P_{\text{th}}$) at various temperatures from 77 to 170 K. The dominant lasing peak red-shifted with a rate of 0.08 nm/K, which could be explained as the refractive index change with the increasing temperature [28]. The lasing output intensity showed no temperature quenching, indicating good temperature reliability. Figure 5(b) plots the L-L curve as a function of temperature under CW operation, indicating the increase of threshold by a factor of ~ 6 and a conspicuous decrease of slope efficiency as temperature rises. Figure 5(c) plots the natural logarithm of threshold power

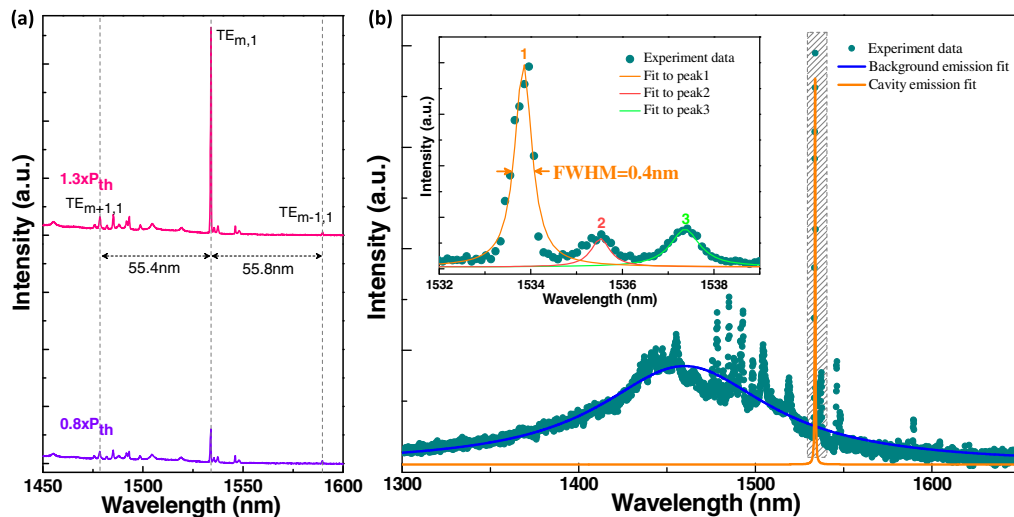


Fig. 4. (a) $\mu\text{-PL}$ spectrum showing transition from sub-threshold emission ($0.8 \times P_{\text{th}}$) to lasing ($1.3 \times P_{\text{th}}$). Output intensity booming can be observed for the WGM at 1534 nm with a well-separated FSR of 55.4 and 55.8 nm. (b) A broad background PL (blue line) accompanied with a narrow cavity emission (orange line) are extracted by a bi-Lorentzian function fit of measured data at $0.8 \times P_{\text{th}}$ pump. Insert: a high-resolution spectrum of the shaded region, indicating the dominant mode linewidth of 0.4 nm.

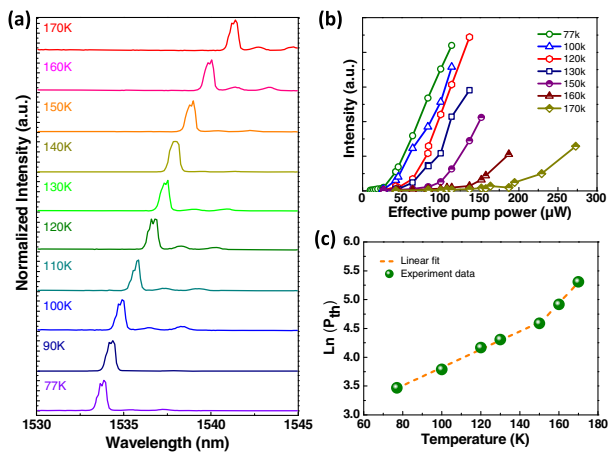


Fig. 5. Temperature-dependent lasing properties of a 4 μm diameter MD. (a) Normalized lasing spectra at 1.3 times the threshold at disparate temperature from 77 to 170 K. The red-shift of lasing peak wavelength is 0.08 nm/K. (b) L-L curves from 77 to 170 K. As temperature rises, an increased threshold and decreased slope efficiency can be identified. (c) Natural logarithm of threshold power against temperature. A characteristic temperature $T_0 = 64$ K in the range of 77–150 K and $T_0 = 28$ K above 150 K is extracted by linear fittings in these two temperature ranges.

as a function of temperature, from which a characteristic temperature $T_0 = 64$ K in the range of 77–150 K and $T_0 = 28$ K above 150 K can be extracted using $P_{\text{th}}(T_2) = P_{\text{th}}(T_1) \exp[(T_2 - T_1)/T_0]$. This value is comparable to the reported T_0 for optically pumped quantum-dot microdisk lasers grown on the III-V substrates [21,29]. Further enhancement of temperature characteristics can be anticipated by optimizing the supporting pedestal diameter to properly balance the heat sinking and optical confinement.

We believe that smaller diameter microdisks are more likely to contribute to dramatic improvement in the threshold. This is attributed to the increased spontaneous emission factor, induced by the reduced number of modes. However, the larger mode spacing in smaller diameter disks makes it arduous to overlap with the background of broad emission from the InAs QDs, leading to a less efficient decoration of the modes by the photons [10]. Also, better laser performance can be expected by engineering the optical quality of QDs in the active region.

In conclusion, we have demonstrated the first 1.55 μm band quantum dot microdisk lasers. Power- and temperature-dependent microphotoluminescence were performed to investigate the lasing characteristics. Continuous-wave lasing with a threshold as low as 32 μW was achieved in the 4 μm diameter disks at liquid nitrogen temperature. Our results demonstrate the advantages of combining small mode volume microdisk cavities with quantum dots, providing better carrier confinement. More significantly, this work marks a major step toward high-performance on-chip light sources and optical interconnects for dense optoelectronics integration and communication networks.

Funding. Research Grants Council, University Grants Committee (RGC, UGC) (16212115, 614813).

Acknowledgment. The authors thank Chak Wah Tang, Qiang Li, Yu Han, Huaxing Jiang, and Yuefei Cai for fruitful discussions, and the staff of the MCPF and NFF of HKUST for their technical support.

[†]These authors contributed equally to this work.

REFERENCES

1. M. Witzany, R. Roßbach, W. Schulz, M. Jetter, P. Michler, T. Liu, E. Hu, J. Wiersig, and F. Jahnke, *Phys. Rev. B* **83**, 205305 (2011).
2. S. L. McCall, A. F. J. Levi, R. E. Slusher, S. J. Pearton, and R. A. Logan, *Appl. Phys. Lett.* **60**, 289 (1992).
3. Y. Ye, Z. J. Wong, X. Lu, X. Ni, H. Zhu, X. Chen, Y. Wang, and X. Zhang, *Nat. Photonics* **9**, 733 (2015).
4. T. Baba and D. Sano, *IEEE J. Sel. Top. Quantum Electron.* **9**, 1340 (2003).
5. J. Van Campenhout, P. Rojo-Romeo, P. Regreny, C. Seassal, D. Van Thourhout, S. Verstuyft, L. Di Cioccio, J.-M. Fedeli, C. Lagahe, and R. Baets, *Opt. Express* **15**, 6744 (2007).
6. D. Chu, M. Chin, N. Sauer, Z. Xu, T. Chang, and S. Ho, *IEEE Photon. Technol. Lett.* **5**, 1353 (1993).
7. C. Seassal, X. Letartre, J. Brault, M. Gendry, P. Pottier, P. Viktorovitch, O. Piquet, P. Blondy, D. Cros, and O. Marty, *J. Appl. Phys.* **88**, 6170 (2000).
8. D. Song, J. Hwang, C. Kim, I. Han, D. Jang, and Y. Lee, *IEEE Photon. Technol. Lett.* **12**, 954 (2000).
9. C. Seassal, P. Rojo-Romeo, X. Letartre, P. Viktorovitch, G. Hollinger, E. Jalaguier, S. Pocas, and B. Aspar, *Electron. Lett.* **37**, 222 (2001).
10. B. Corbett, J. Justice, L. Considine, S. Walsh, and W. Kelly, *IEEE Photon. Technol. Lett.* **8**, 855 (1996).
11. A. C. Tamboli, E. D. Haberer, R. Sharma, K. H. Lee, S. Nakamura, and E. L. Hu, *Nat. Photonics* **1**, 61 (2007).
12. R. Slusher, A. Levi, U. Mohideen, S. McCall, S. Pearton, and R. Logan, *Appl. Phys. Lett.* **63**, 1310 (1993).
13. Z. Liu, J. M. Shainline, G. E. Fernandes, J. Xu, J. Chen, and C. F. Gmachl, *Opt. Express* **18**, 19242 (2010).
14. S. Chen, W. Li, J. Wu, Q. Jiang, M. Tang, S. Shutts, S. N. Elliott, A. Sobiesierski, A. J. Seeds, I. Ross, and P. M. Smowton, *Nat. Photonics* **10**, 307 (2016).
15. K. Srinivasan, M. Borselli, T. J. Johnson, P. E. Barclay, O. Painter, A. Stintz, and S. Krishna, *Appl. Phys. Lett.* **86**, 151106 (2005).
16. Y. Wan, Q. Li, A. Y. Liu, A. C. Gossard, J. E. Bowers, E. L. Hu, and K. M. Lau, *Opt. Lett.* **41**, 1664 (2016).
17. I. Aharonovich, A. Woolf, K. J. Russell, T. Zhu, N. Niu, M. J. Kappers, R. A. Oliver, and E. L. Hu, *Appl. Phys. Lett.* **103**, 021112 (2013).
18. T. Katsuyama, *SEI Tech. Rev.* **69**, 13 (2009).
19. B. Shi and K. M. Lau, *J. Cryst. Growth* **433**, 19 (2016).
20. J. Lothian, F. Ren, and S. Pearton, *Semicond. Sci. Technol.* **7**, 1199 (1992).
21. T. Ide, T. Baba, J. Tatebayashi, S. Iwamoto, T. Nakaoka, and Y. Arakawa, *Opt. Express* **13**, 1615 (2005).
22. Y. Chu, A. Mintairov, Y. He, J. Merz, N. Kalugnyy, V. Lantratov, and S. Mintairov, *Phys. Status Solidi C* **8**, 325 (2011).
23. G. Bjork and Y. Yamamoto, *IEEE J. Quantum Electron.* **27**, 2386 (1991).
24. Y. Chu, A. Mintairov, Y. He, J. Merz, N. Kalyuzhnyy, V. Lantratov, and S. Mintairov, *Phys. Lett. A* **373**, 1185 (2009).
25. D. Lebedev, A. Mintairov, M. Kulagina, S. Troshkov, J. Kapaldo, J. Merz, S. Rouvimov, G. Juska, A. Gocalinska, and S. Moroni, *J. Phys. Conf. Ser.* **690**, 012023 (2016).
26. N. Frateschi and A. Levi, *Appl. Phys. Lett.* **66**, 2932 (1995).
27. J. Shainline, S. Elston, Z. Liu, G. Fernandes, R. Zia, and J. Xu, *Opt. Express* **17**, 23323 (2009).
28. J. Tatebayashi, S. Kako, J. Ho, Y. Ota, S. Iwamoto, and Y. Arakawa, *Nat. Photonics* **9**, 501 (2015).
29. T. Yang, A. Mock, J. D. O'Brien, S. Lipson, and D. G. Deppe, *Opt. Express* **15**, 7281 (2007).